Structure of Human Acid Sphingomyelinase Reveals the Role of the Saposin Domain in Activating Substrate Hydrolysis

Zi-Jian Xiong[1], Jingjing Huang[1], Gennady Poda[2,3],
Régis Pomès[1,4] and Gilbert G. Privé[1,5,6]

1 - Department of Biochemistry, University of Toronto, Toronto, Ontario, Canada
2 - Drug Discovery, Ontario Institute for Cancer Research, Toronto, Ontario, Canada
3 - Leslie Dan Faculty of Pharmacy, University of Toronto, Toronto, Ontario, Canada
4 - Molecular Structure and Function, Hospital for Sick Children, Toronto, Ontario, Canada
5 - Department of Medical Biophysics, University of Toronto, Toronto, Ontario, Canada
6 - Princess Margaret Cancer Centre, Toronto, Ontario, Canada

Correspondence to Gilbert G. Privé: Princess Margaret Cancer Centre, 101 College Street, Toronto, Ontario, Canada, M5G 1L7. prive@uhnres.utoronto.ca
http://dx.doi.org/10.1016/j.jmb.2016.06.012
Edited by J. Bowie

Abstract

Acid sphingomyelinase (ASM) is a lysosomal phosphodiesterase that catalyzes the hydrolysis of sphingomyelin to produce ceramide and phosphocholine. While other lysosomal sphingolipid hydrolases require a saposin activator protein for full activity, the ASM polypeptide incorporates a built-in N-terminal saposin domain and does not require an external activator protein. Here, we report the crystal structure of human ASM and describe the organization of the three main regions of the enzyme: the N-terminal saposin domain, the proline-rich connector, and the catalytic domain. The saposin domain is tightly associated along an edge of the large, bowl-shaped catalytic domain and adopts an open form that exposes a hydrophobic concave surface approximately 30 Å from the catalytic center. The calculated electrostatic potential of the enzyme is electropositive at the acidic pH of the lysosome, consistent with the strict requirement for the presence of acidic lipids in target membranes. Docking studies indicate that sphingomyelin binds with the ceramide-phosphate group positioned at the binuclear zinc center and molecular dynamic simulations indicate that the intrinsic flexibility of the saposin domain is important for monomer-dimer exchange and for membrane interactions. Overall, ASM uses a combination of electrostatic and hydrophobic interactions to cause local disruptions of target bilayers in order to bring the lipid headgroup to the catalytic center in a membrane-bound reaction.

Introduction

Sphingomyelin (SM) is the most abundant sphingolipid in the plasma membrane of most eukaryotic cells, and is especially enriched in neural tissue [1]. SM has important roles in determining the physical properties of biological membranes, and serves as a source for the bioactive signaling lipid ceramide [2]. SM is synthesized in the endoplasmic reticulum (ER) and Golgi, and is ultimately trafficked to the outward-facing leaflet of the plasma membrane [3]. Along with other sphingolipids, SM is internalized by endocytocytic pathways and is directed to lysosomes for catabolic breakdown. In the lysosome, sphingolipids are degraded by a series of reactions carried out by a panel of lysosomal hydrolases that ultimately convert these lipids into sphingosine and other basic components [4]. Many of these reactions take place at the water-membrane interface of luminal intralysosomal vesicles with the aid of a set of small lipid binding proteins, the sphingolipid activator proteins, or saposins [5]. Acid sphingomyelinase (ASM, product of the SMPD1 gene) is a lysosomal phosphodiesease that catalyzes the hydrolysis of SM to produce ceramide and phosphocholine, but does not require a saposin cofactor;

instead, the ASM polypeptide includes a built-in N-terminal saposin domain [6].

ASM is implicated in several clinically important aspects of human health. Inherited deficiencies of ASM activity results in the massive accumulation of SM in lysosomes and lead to the severe lysosomal disorders Niemann-Pick disease, types A and B (NPD-A, NPD-B) [7]. NPD-A is characterized by a rapid progressive neurogeneration and is invariably lethal in early childhood. These patients are characterized by a complete or near-complete loss of ASM activity. NPD-B has later onset involving visceral organ abnormalities but with little or no neurological symptoms, and typically ASM activity levels of 5–20% of normal can be detected. In addition, ASM produces the bioactive and pro-apoptotic lipid ceramide, which is linked to stress and inflammation. Tricyclic antidepressants (TCAs) are inhibitors of ASM have been used to treat many neuronal diseases such as major depression [8] and may find applications in Alzheimer's disease [9]. In cancer cells, low levels of ASM activity produces fragile lysosomes due to high SM levels, and ASM inhibitors can induce lysosomal membrane permeabilization and trigger cell death pathways [10].

ASM is first generated as a 75 kDa prepro-protein and is directed to two distinct post-translational trafficking pathways within the ER-Golgi network. The extracellular secreted form (s-ASM) is produced via the phosphorylation of S508 [11,12], and the lysosomal form (l-ASM, here simply ASM), is targeted to endolysosomal compartments via the mannose-6-phosphate pathway or sortilin [13]. Within the lysosome, ASM is further processed by lysosomal proteases that removes residues at both the N- and C-termini of the chain, including an autoinhibitory C-terminal cysteine [14]. The mature lysosomal form of ASM is a 70 kDa protein with six N-linked glycosylation sites and 8 intrachain disulphide bonds. Mature ASM consists of an N-terminal saposin domain, a proline-rich domain, and a metallophosphoesterase catalytic domain which includes a family-specific C-terminal α-helical region. While several lysosomal hydrolases require saposins as cofactors for their *in vivo* activity [4,5], the degradation of SM by ASM is not affected in prosaposin deficiency patients possibly due to the presence of its internal saposin domain [15]. Thus, ASM may act as a "performed" saposin/enzyme complex and may provide insight into the mechanism of saposin activation of the other lysosomal sphingolipid hydrolases. In addition to its activity in SM hydrolysis, ASM is a relatively non-specific phosphodiesterase and can also hydrolyze phosphatidylcholine (PC), phosphatidylglycerol (PG) and other phospholipids [16–18].

ASM orthologs containing the saposin, connector and catalytic domains are present in most metazoans as well as in some fungi and ameobas. ASM-like proteins are also known, notably SMPDL3A and SMPDL3B, but these do not include the saposin or connector regions. These ASM paralogs also have phosphodiesterase activity, and the former can hydrolyze nucleotides but not SM [19], while the latter may generate ceramide from SM [20], although this has not yet been directly demonstrated.

Here, we present the crystal structure of human ASM and characterize its interactions with liposomes of defined composition. In agreement with previous reports, we find that lipid binding requires both an acidic environment and the presence of acidic lipids, but is not dependent on SM. Molecular dynamics and docking studies based on the crystal structure provide an atomistic view of how ASM interacts with its substrates and bilayer surfaces, and suggests how the saposin domain leads to local disruptions of the lipid structure. Overall, these results support a reaction mechanism that brings the target phosphoester bond of the lipid headgroup to the dinuclear zinc active site in a reaction localized at membrane surfaces.

Results and discussion

Structure of ASM

We determined the crystal structure of human ASM to 2.8 Å resolution (Figs. 1, S1 and Table 1). Recombinant protein was secreted from stable HEK293 GnT1$^{-/-}$ cells generated with a *piggyBac* transposon-based expression system [21]. The natural N-terminal signal sequence from residues 1–46 was replaced with an artificial secretion signal sequence, and the C-terminal autoinhibitory cysteine 629 was substituted with a serine [22]. Glycosylated recombinant protein was purified from conditioned medium and crystallized. Residues 47–81 and 612–629 from the termini of the protein are disordered in the crystals and were not modeled, and the final refined model consists of residues 83–611. We were able to model partial carbohydrate structures at all six of the predicted N-glycosylation sites. There are two copies of the enzyme in the crystallographic asymmetric unit, and the two chains superimpose with a Cα RMSD of 0.19 Å for residues 83–611.

ASM consists of three distinct regions: a saposin domain from residues 83–165, a connector region from 166 to 198, and a catalytic domain from 199 to 611 (Fig. 1). The saposin and catalytic domains share 27% and 31% sequence identity with human saposin A and SMPDL3A, respectively, while the connector region has no significant sequence similarity to any of the sequences from proteins in the protein data bank (PDB). Overall, the enzyme has the shape of a large shallow bowl, with a raised,
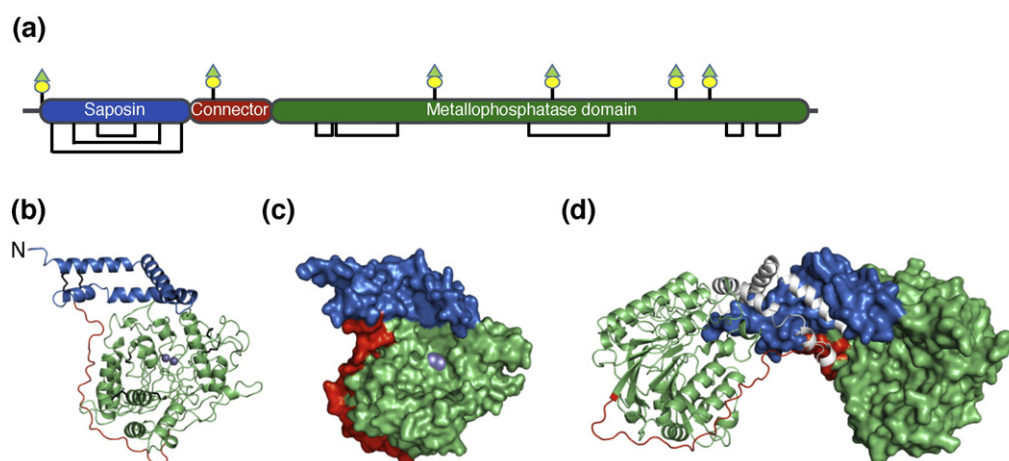
Fig. 1. Structure of ASM. (a) Domain organization of ASM, indicating the glycosylation sites and disulfide bonds. (b,c) Crystal structure of ASM in ribbon and surface representation, with coloring as in panel (a). Disulfide bonds are shown as black lines, and the zinc ions at the active site are shown as grey spheres. (d) ASM homodimer in the crystal formed by the association of the two saposin domains. One chain is represented as a surface and the other as a ribbon with a gray saposin domain.

Table 1. Crystallographic data and model refinement statistics.

	Native		Seleomethionine-substituted
	Sphere	Elliptically truncated[a]	Sphere
Data collection	MacCHESS A1	MacCHESS A1	CLS CMCF 08ID
Wavelength (Å)	0.63	0.63	0.979
Resolution range (Å)[b]	26.8–2.8 (2.9–2.8)	26.8–2.8 (2.9–2.8)	48.3–3.03 (3.16–3.03)
Space group	P $2_12_12_1$	P $2_12_12_1$	P $2_12_12_1$
Cell parameters			
a, b, c (Å)	69.5, 143.7, 193.6	69.5, 143.7, 193.6	68.7, 143.4, 193.2
α, β, γ (°)	90, 90, 90	90, 90, 90	90, 90, 90
Unique reflections	45,778 (3534)	36,062 (358)	37,957 (4575)
Completeness (%)	94 (73)	74 (7)	99.9 (99.8)
Redundancy	3.9 (2.8)	4.0 (3.3)	10.1 (10.4)
Mean I/sigma	7.7 (0.67)	9.57 (2.04)	9.4 (0.6)
R_{merge}	0.209 (2.29)	0.161 (0.91)	0.178 (4.93)
R_{merge} in top intensity bin	0.058	0.058	0.052
R_{meas}	0.236 (2.694)	0.184 (1.08)	
$CC_{1/2}$	0.989 (0.245)	0.998 (0.572)	0.998 (0.263)
CC_{anom}	-	-	0.260[c]
Refinement			
Reflections: work/free	45,556/1975		
R_{work}/R_{free}	0.23/0.28		
Number of atoms			
Protein	8,343		
Carbohydrate	287		
Zinc	4		
Average B factors (Å²)	61.6		
Protein	60.3		
Carbohydrate	99.4		
Metal	72.4		
R.M.S.D			
Bond length (Å)	0.004		
Bond length (°)	0.93		
Ramachandran outliers (%)	0.38		

[a] Values for a dataset truncated to a resolution of 3.4 Å, 3.0 Å and 2.8 Å along the a*, b* and c* direction, respectively.
[b] Values in parentheses are calculated for the high resolution shell.
[c] Values for the resolution range 48.3–5.57 Å.

arc-shaped lip along one edge, which is made up of an open-form of the saposin domain. The active site of the enzyme is at the center of the bowl, and the six glycosylation sites are located on the back side of the bowl. The burial of the saposin inner concave surface with a second saposin domain from the partner chain generates a homodimer in the crystalline state.
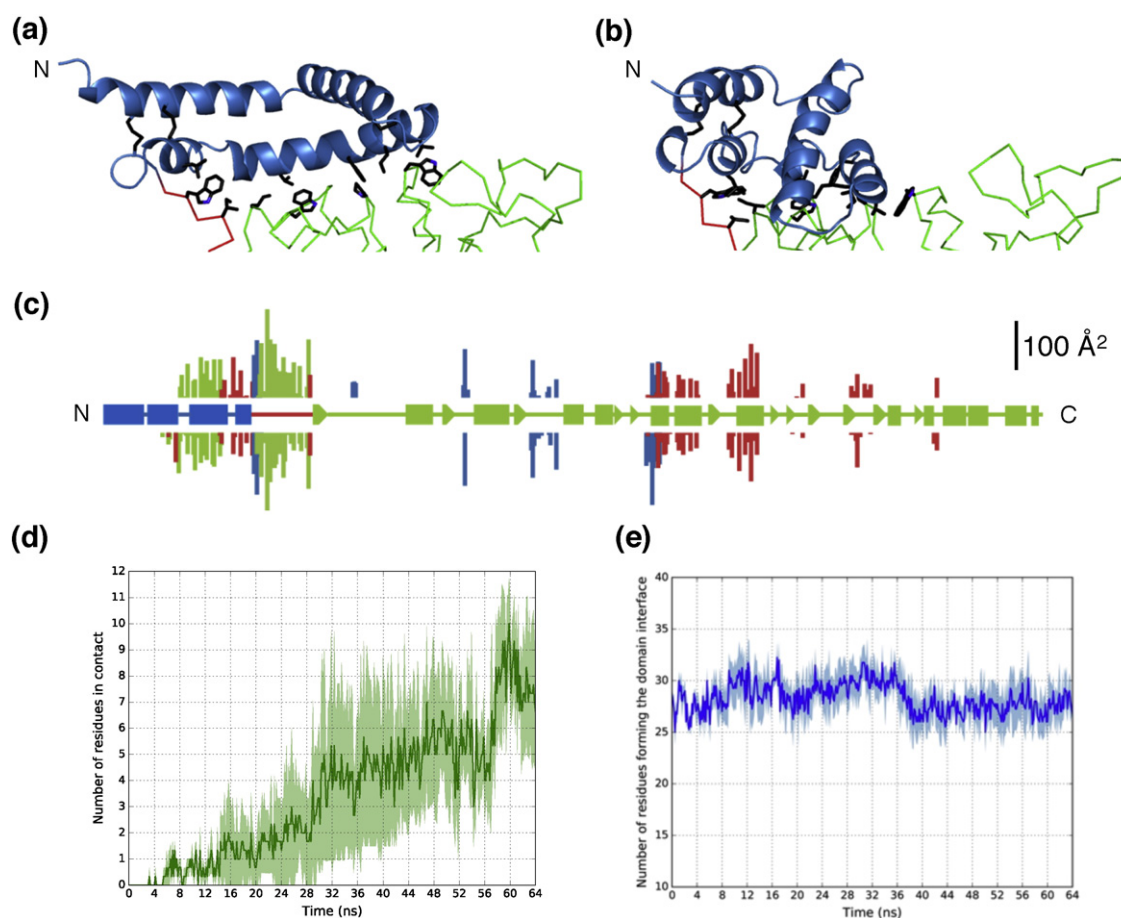
Saposin domain and ASM dimer

The saposin domain shares similar secondary structure elements with other saposin proteins, and consists of four α-helices stabilized by three disulphide bonds. A sequence alignment of the ASM saposin domain and other saposins reveals a similar distribution of polar and hydrophobic residues (Fig. 2a). The ASM saposin domain adopts a V-shaped conformation formed by the stem helices (α1 and α4) and the hairpin helices (α2 and α3) with a hinge opening of approximately 90° exposing an inner hydrophobic concave surface (Fig. 2b). The domain is tightly associated with the rest of the protein through extensive contacts along the lower "edge" of the V, involving saposin helix α3 with the catalytic domain and helix α4 with the connector region (Fig. 3a). This contact region involves evolutionarily conserved hydrophobic residues from the saposin, connector and catalytic domain regions (Fig. 4). Within each ASM chain, the interdomain contact surface engages residues V130, I134, L137, F138, D141, V145, R148, and L159 from the saposin domain and residues W168, I170, W285, P323, F390, W391, L393, I394 from the connector region and catalytic domain, burying a total area of 1100 Å^2. The equivalent surface of the catalytic
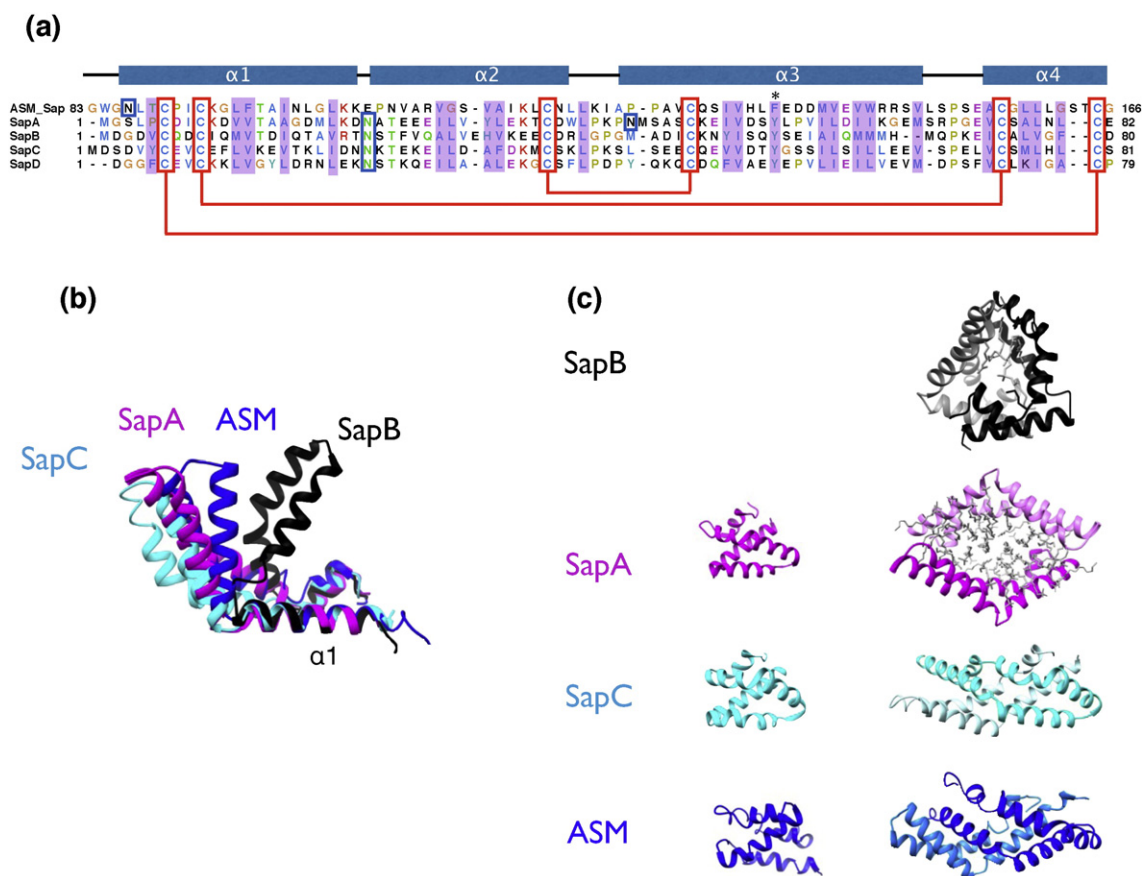
Fig. 2. Conformational flexibility in the saposins. (a) Sequence alignment of the saposin domain from ASM with human saponins A-D. Conserved disulfide bonds are indicated with red boxes, and conserved hydrophobic residues are shaded in purple. Asparagine residues of N-linked glycosylation sites are indicated in blue boxes. The helix α3 aromatic position that forms a kink upon saposin closure of is labeled "*". Residues are colored according to conservation and similarity. (b) Structural comparison of the indicated saposins from the open form dimeric states aligned through helix α1 of the stem region. (c) Monomeric saposins show a hinge opening change upon dimerization. Crystal structures are shown for monomeric and dimeric structures of saposin A (2DOB and 4DDJ), saposin C (2GTG and 2QYP), and ASM (this work; the monomer is based on the MD calculations and the dimer is from the crystal structure). SapB (1N69) is found exclusively as a homodimer. Bound lipids and detergents observed in the crystal structures are colored in grey.

Fig. 3. Conformational flexibility in the saposin domain and intrachain contacts. (a) Open-state saposin from the crystal structure and (b) closed monomeric state from MD simulations. Coloring as in Fig. 1. Selected residues involved in interdomain contacts are shown as black sticks. (c) Secondary structure schematic of ASM with the saposin domain in blue, linker in red and catalytic domain in green. The histograms show the intrachain residue contacts colored according to the binding region. The upper histogram is the buried surface area calculated for the open saposin state (crystal). The lower histogram shows the interdomain buried surface areas for the closed state (MD). Most contacts are preserved upon closure of the saposin domain. Statistics of the all-atom MD simulations of the ASM monomer in water: (d) The time evolution of closure of the saposin domain, as measured by the number of contacts between the stem helices and the hairpin helices. (e) The time evolution of the average number of residues forming the domain interface between the saposin domain and the connector + catalytic domain remained fairly constant over the three simulations with closure. The starting configuration was generated from the crystal structure with an open saposin conformation. Four 64 ns systems were were simulated, and the statistics reflect the average of three three simulations that showed closure of the saposin domain. The transparent shading indicates the standard deviation of the mean.

domain in ASML3A, which does not include a saposin or connector domain but is otherwise similar to ASM, is hydrophilic and includes a cluster of charged residues. This close association between the saposin domain and the rest of the protein is consistent with the previous characterization of saposin domain in ASM by mutagenesis [23].

A range of hinge angles have been observed in the other saposin proteins, ranging from closed monomeric states which bury a small hydrophobic core, to open states which expose a concave hydrophobic surface (Fig. 2b,c) [24–28]. In all cases, open state saposins interact with lipids, detergents or with each other through the exposed hydrophobic surface.

Consistent with this, the concave surface of the open saposin domain of ASM is not exposed to solvent, but is instead buried by forming a homodimer with the saposin domain from the other ASM chain in the crystal (Figs. 1, 2c).

Although we observe a dimer in the crystal state, ASM is predominantly monomeric in solution at µM concentrations (Fig. S2). We carried out molecular dynamics (MD) simulations on the solvated monomer in order to gain insight into the behaviour of the saposin domain upon dissociation of the ASM dimer. While the linker and catalytic domains remained stable over the course of four independent 64 ns simulations, the saposin domain underwent a
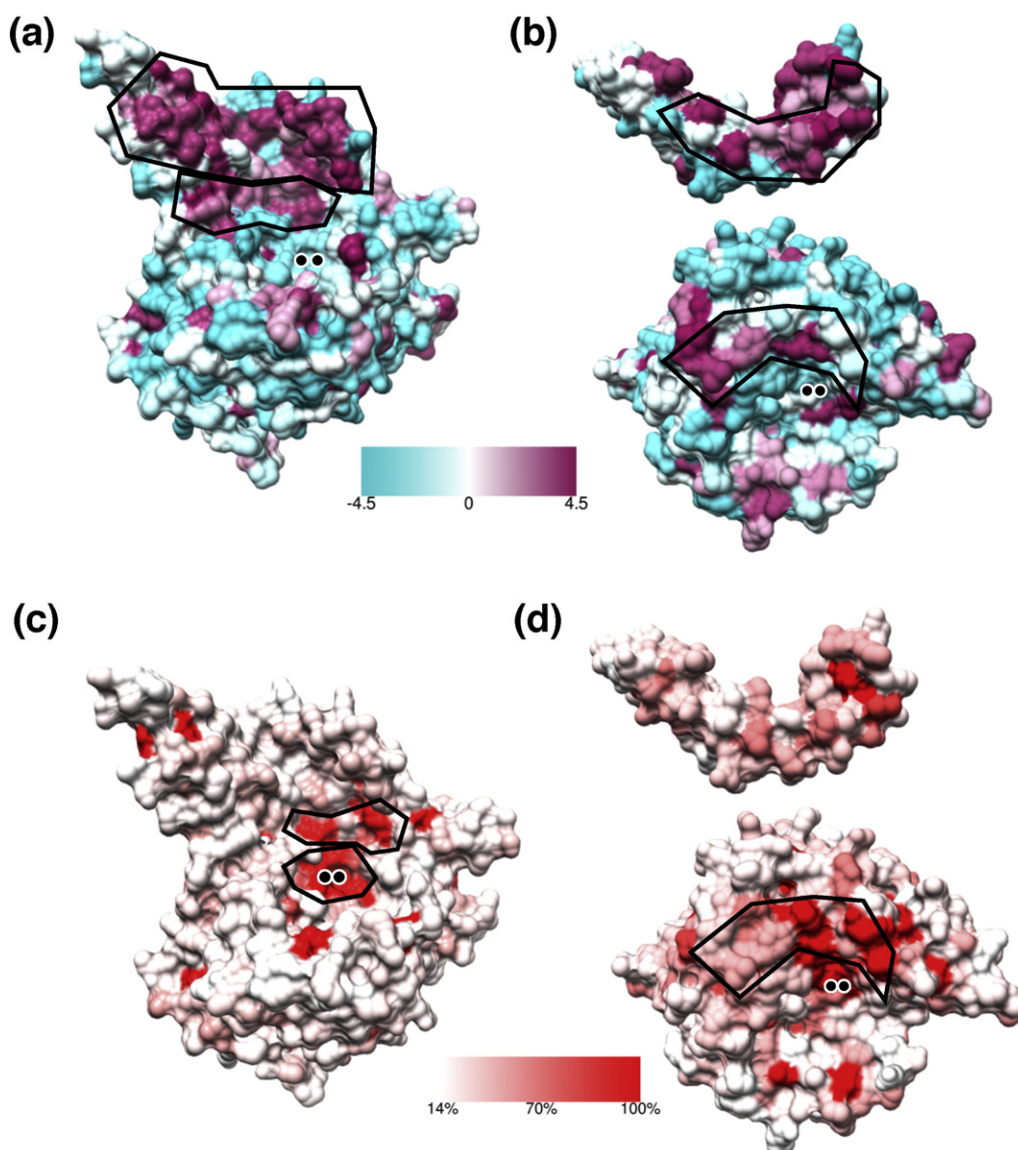
Fig. 4. Surface representations of ASM as seen in the crystal conformation. (a) Surface colored according to hydrophobicity shows the nonpolar inner surface of saposin domain (upper boxed region; buried by saposin-saposin contacts in the dimer) and a nonpolar surface located between the saposin domain and the catalytic center (lower boxed region; this region is solvent exposed in both the dimer and MD monomer structure with a closed saposin). The di-zinc metal center is indicated by two black circles. (b) Clamshell-opened view of the hydrophobic interface between the saposin domain and the catalytic domain. The boxed regions highlight the buried interface from both domains. (c) ASM sequence conservation mapped onto the protein surface shows the high conservation surrounding the active site and at the saposin/catalytic domain interface (boxed regions). (d) Clamshell-opened view of the sequence-conserved interface between the saposin domain and the catalytic domain.

conformational transition from the initial open state from the crystal structure to a closed state in three of the four replicates (Fig. 3). Saposin closure leads to the burial of the exposed hydrophobic residues lining the concave surface while maintaining the conserved hydrophobic contacts between the saposin helices α3 and α4 and the connector and catalytic domains (Fig. 3b,c). Furthermore, saposin closure involved hinge motions in the α1/α2 loop and at a conserved

aromatic site midway through helix α3 (Fig. 2c), which are very similar to the changes seen in comparing the open and closed states of saposins A and C [24,26,28]. We note, however, that the hairpin closure in the ASM saposin domain is in the opposite direction of that seen in the saposin monomers [28,29]. Remarkably, the majority of the contacts between the saposin domain and the rest of the enzyme are preserved in the saposin-
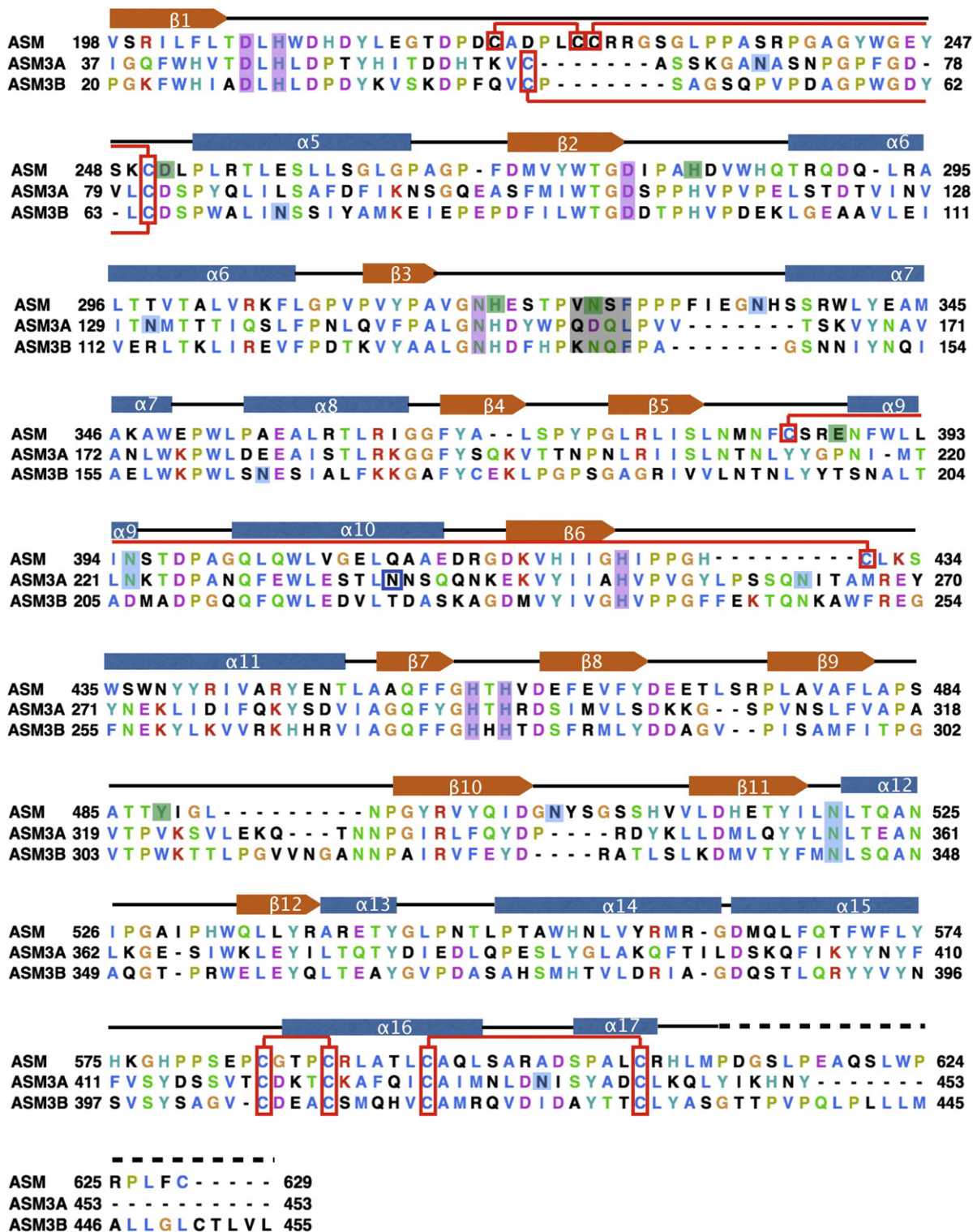
Fig. 5. Structure-based multiple sequence alignment of the ASM catalytic domain with human SMPDL3A (ASM3A) and SMPDL3B (ASM3B). Disulfide bonds are indicated with red boxes. Zinc coordinating residues are highly conserved and are shaded in magenta. N-link glycosylation sites are shaded in blue. Conserved ASM residues likely to be involved in substrate binding and/or the hydrolysis reaction are shaded in green. The "VNSF" motif is shaded in black (see text). The ASM secondary structure is indicated above the alignment and is conserved in SMPDL3A. The disordered C-terminal region is indicated with a dashed line. Residues are colored according to conservation and similarity.
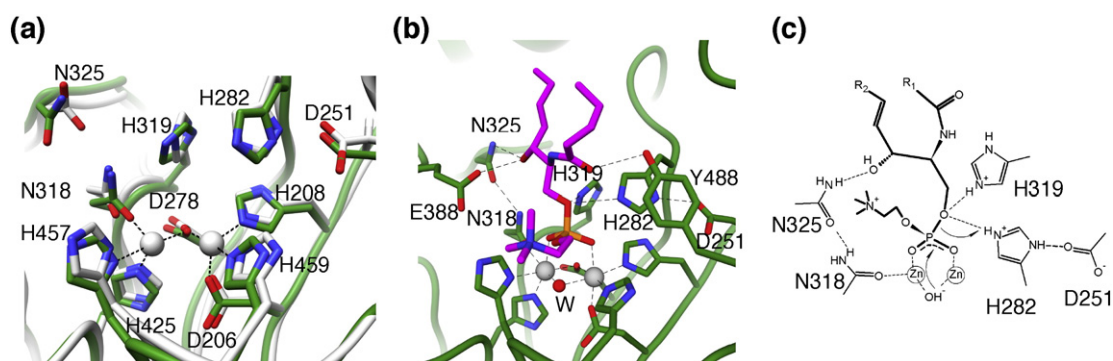
Fig. 6. Geometry of the ASM active site. (a) Superimposed view of the ASM (green carbons) and SMPDL3A (PDB ID 5FC5; white carbons) active site showing the coordination of the two Zn^{2+} metal ions (gray spheres). Residue numbering is for ASM. Residues D251, H282, H319, N325 do not directly coordinate the zinc ions but are proposed to be involved in substrate interaction. (b) Docked complex of a short-chain SM analog (magenta carbons). "W" indicates a water/hydroxyl group that is not modeled in the ASM crystal structure. (c) Schematic drawing of the docked SM indicating proposed reaction mechanism and the predicted contacts between the substrate and evolutionarily conserved protein residues. It is not clear whether H282 or H319 acts as the general acid.

closed state of ASM, since most of these are C-terminal to the kink site at F138 in helix α3 (Fig. 3c). Overall, ASM exists in a monomer/dimer equilibrium in solution at pH 5 as a result of flexibility in the saposin domain. We believe that the monomer is the catalytically relevant form of the enzyme, as described in more detail below.

Connector

The connector region spans residues 167–198 and follows an extended, 80 Å long L-shaped path along the backside of the catalytic domain with a buried surface area of 1406 Å^2. Despite the absence of any regular secondary structure, all of the residues in this region have clear electron density and atomic displacement parameters (ADPs) that are similar to those of the saposin and catalytic domain (Fig. S1a, b). The N-terminal region of the connector forms close hydrophobic contacts with helix α4 of the saposin domain and helices α10 and α11 of the catalytic domain, mainly through residues W168, I170, F171, W174, I176 and L178. Over half of the residues in the second half of the connector are proline residues, and this region associates with the catalytic domain through a series of polar and non-polar interactions. Given the high degree of order of the connector, the close contacts with the main body of the protein, and the structural similarity between the two crystallographically independent chains, we consider this region as rigidly and stably associated with the main body of the protein.

Catalytic domain

The core of the catalytic domain consists of two 6-stranded β-sheets surrounded by a ring of α-helices, which is the signature fold for the family of

calcinerurin-like phosphoesterases (PFAM code: PF00149). The set of α-helices and loops form a bowl-shaped surface around the binuclear zinc ions, which are tightly coordinated by residues from the loops following strands β1, β2, β3, β6 and β7. The overall structure is similar to the recently reported structures of SMPDL3A [30,31]. In addition, ASM and SMPDL3A include two subdomains that are unique to this class of phosphoesterases: a cysteine-rich loop region and a C-terminal helical region (spanning residues 213–252 and 549–611 in ASM, respectively). Notably, the ASM cysteine-rich loop includes an additional non-equivalent disulphide bond not present in SMPDL3A (Fig. 5), and adopts a considerably different conformation from SMDL3A, despite having a related topology. The role of this loop is not clear, but sixteen known NPD mutations are located in this region (Fig. S3), suggesting an important role for ASM folding and/ or activity. The active face of the SMPDL3A enzyme has been described as a V-shaped pocket [30] or a T-shaped cavity [31]. ASM, in contrast, presents a wider, bowl-shaped active surface. The main differences in the shape of the proximal face of the enzyme are due to 1) the saposin domain, 2) the reorganized cysteine-rich loop and 3) shorter loops between β6-α11 and β9-β10 (Fig. 5). The net result is a shallower environment surrounding the catalytic center of ASM.

Active site

The ASM dimetal zinc center is coordinated by D206, H208, D278, N318, H425, H457 and H459, and equivalent residues are found in the SMPDL3A metal center (Figs. 5, 6a) [29,30]. As with other phosphoesterases from the calcinerurin-like super-family, the dimetal zinc center of SMPDL3A has been proposed to coordinate the two unesterified oxygen atoms of the substrate phosphodiester as well as the

nucleophilic water or hydroxyl [31]. This arrangement is consistent with the structure we describe here, although we do not observe the attacking water/hydroxyl in our structure.

We carried out molecular docking calculations in order to gain insight into substrate binding in ASM. We used a SM analogue with truncated acyl tails in order to reduce the size and complexity of the ligand and improve conformational sampling. A water was positioned 2.0 Å from the two zinc ions opposite the D278 carboxylic oxygen, as has been observed in multiple SMPDL3A structures [31]. The top scoring pose placed the two unesterified oxygen atoms of the SM phosphate group at the di-zinc center (Fig. 6b), equivalent to the arrangement seen in a SMPDL3A/AMP co-crystal (PDB ID 5FC5) [31]. Notably, this arrangement positioned the phosphate atom at a position suitable for attack by the zinc-activated nucleophile (Fig. 6c). Several evolutionarily conserved polar residues, including H319, H282, N325 and D251, are located in the vicinity of the zinc site and may be involved in ligand recognition and substrate positioning. Mutations affecting several of these residues have been identified in NPD patients (Fig. S3). We note that E388 and Y488 are also near the site and may engage the substrate, but are unlikely to be essential for the activity of the enzyme because they are not conserved in ASM orthologs (Fig. S4).

Asparagine 325 is solvent exposed and forms a hydrogen bond to the sphingosine hydroxyl in our docked SM complex. This residue is found in a highly conserved 324-VNSF-327 sequence motif in ASM orthologs (Fig. S4), but this sequence signature is not present in SMPDL3A and B (Fig. 5). The equivalent residue in SMPDL3B is N140, and this enzyme may be a sphingomyelinase, since it has significant impacts on ceramide and sphingomyelin level *in vivo* [20]. SMPDL3A and the ASM-like enzyme from *Ralstonia solanacearum*, on the other hand, have an aspartate at this position and are nucleotide hydrolases but cannot hydrolyze sphingomyelin, even in micelle-based assays [19,30,32]. We propose that the N325 has a key role in SM recognition and forms a hydrogen bond with either the hydroxyl group of the sphingosine chain or the amide linkage with the fatty acyl chain (or alternatively, with the glycerol ester linkage of a glycerophospholipid), and helps to orient the phosphodiester of the lipid in the active site with the acyl chains directed toward the saposin domain.

The docked structure orients the cholate moiety of the SM phosphodiester away from the saposin side of the bowl, making only superficial contacts with the surrounding floor of the protein. The remaining ester oxygen that forms the linkage to the ceramide group was positioned 3.0 Å from the pyridine-like nitrogens of H282 and H319 (equivalent to H114 and H152 in human SMPDL3A). ASM generates phosphocholine

and ceramide from sphingomyelin, and thus the docked molecule placed the appropriate target phosphoester linkage at the expected position in the active site. In the protonated form, H282 would participate in a charge relay with the highly conserved residue D251, suggesting that H282 may serve as the general acid for protonation of the ester oxygen. We note that while highly conserved, this residue is a glycine in several fungal ASM enzymes (Fig. S4). H319, however, appears to be absolutely conserved in all ASM paralogs sequenced to date, and this residue should also be considered as a candidate for the general acid.

Lipid binding

We conducted liposome pull-down assays to examine the membrane binding requirements for ASM. Consistent with previous reports [16], ASM required two of the conditions present in lysosomes for vesicle binding: acidic pH and the presence of the anionic lipid bis(monoacylglycero)phosphate (BMP) in the target membrane (Figs. 7a, S5). We tested the effect of the cationic amphiphile desipramine, a TCA, on ASM liposome binding. TCAs are weak bases that act as functional inhibitors of ASM by accumulating within lysosomes and BMP-containing intralysosomal vesicles [33]. These inhibitors reduce the net negative charge of the membranes, resulting in the release of ASM into the lysosomal lumen where the enzyme is degraded by cathepsins and other proteases [34]. As expected, desipramine reduced ASM binding to BMP-containing vesicles in a dose-dependent manner (Fig. 7b). Furthermore, the catalytic activity of ASM was highly correlated with membrane association (Fig. 7c). These observations are consistent with previous conclusions that ASM is tightly associated with membrane surfaces in the lysosome, and that binding is predominantly driven by electrostatic effects [16] with its highly positively charged surface at lysosomal pH (Fig. S6).

Disease mutations

We mapped the NPD mutations [35] onto the structure of ASM and grouped these according to their location in the enzyme (Fig. S3). Overall, disease mutations are distributed throughout the protein. The two β-sheets that form the core of ASM are mostly hydrophobic and position the loops that contain the active-site residues as well as provide the association surface for the outer α-helices. Accordingly, many NPD-A and NPD-AB mutations affect hydrophobic residues that localize to the core sheet region, and likely destabilize the protein. Several mutations are found in the flanking α-helices, and most of these map to buried interfaces with other helices or sheets. NPD-A mutations H319Y, H425R and D278A affect the conserved residues of the

(a) **(b)** **(c)**
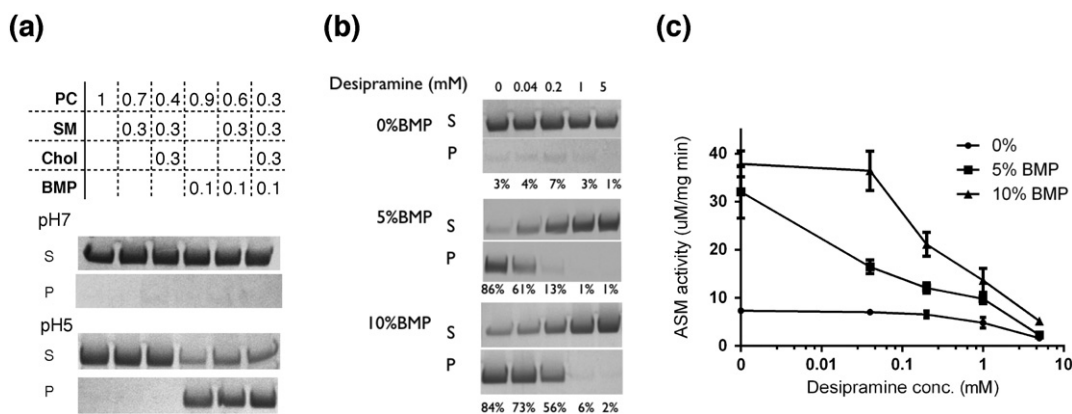
Fig. 7. Liposome binding and activity. (a) ASM bound in liposome pellet (P) or unbound in supernatant (S) was measured by SDS-PAGE with Coomassie blue staining. Liposomes with the indicated mole fraction compositions were tested at neutral and acidic pH (PC: phosphatidylcholine, Chol: cholesterol). (b) The cationic amphiphilic drug desipramine inhibits ASM binding to BMP-containing liposomes (30% SM, 5% cholesterol, 0–10% BMP and 55%–65% PC) at pH 5. Liposome binding was quantitated by densitometry of stained gels, and is indicated below the images. The experiment was repeated three times; a representative result is shown. (c) ASM activity was measured by phosphocholine release from liposomes with lipid compositions as in panel (b). The error bars represent the standard error of the mean based on six replicates.

active site and accordingly, result in a complete loss of ASM activity. Loss of the disulfide linkage near the active site in the C385R and C431R mutations (Fig. S3) may deform the region near the substrate binding pocket, but it is curious that C385R has a much more severe effect than C431R. These two cysteines are not conserved in all ASM orthologs (Fig. S4) however, and single disease mutations involving only C385 or C431 would result in an unpaired cysteine with possible deleterious consequences. Mutations in the saposin domain or the connector generally do not lead to a complete loss of function, with the notable except of P184L, which is located at the turning point of the "L" shaped connector and there may be a strict requirement of this residue for ASM folding. Mutations in the catalytic domain that form the interface to saposin domain are, however, more potent. Examples include the NPD-A mutations W209R, F390Δ and Y446C, supporting the suggestion that the tight association between the saposin domain and the catalytic domain is essential for proper ASM function. Notably, a concentration of NPD mutations are located in the cysteine-rich loop between β1 and α5, and 13 mutations have been identified in this 30 residue segment, including C226R, R228C and W244C, which would affect disulfide bond formation in this region.
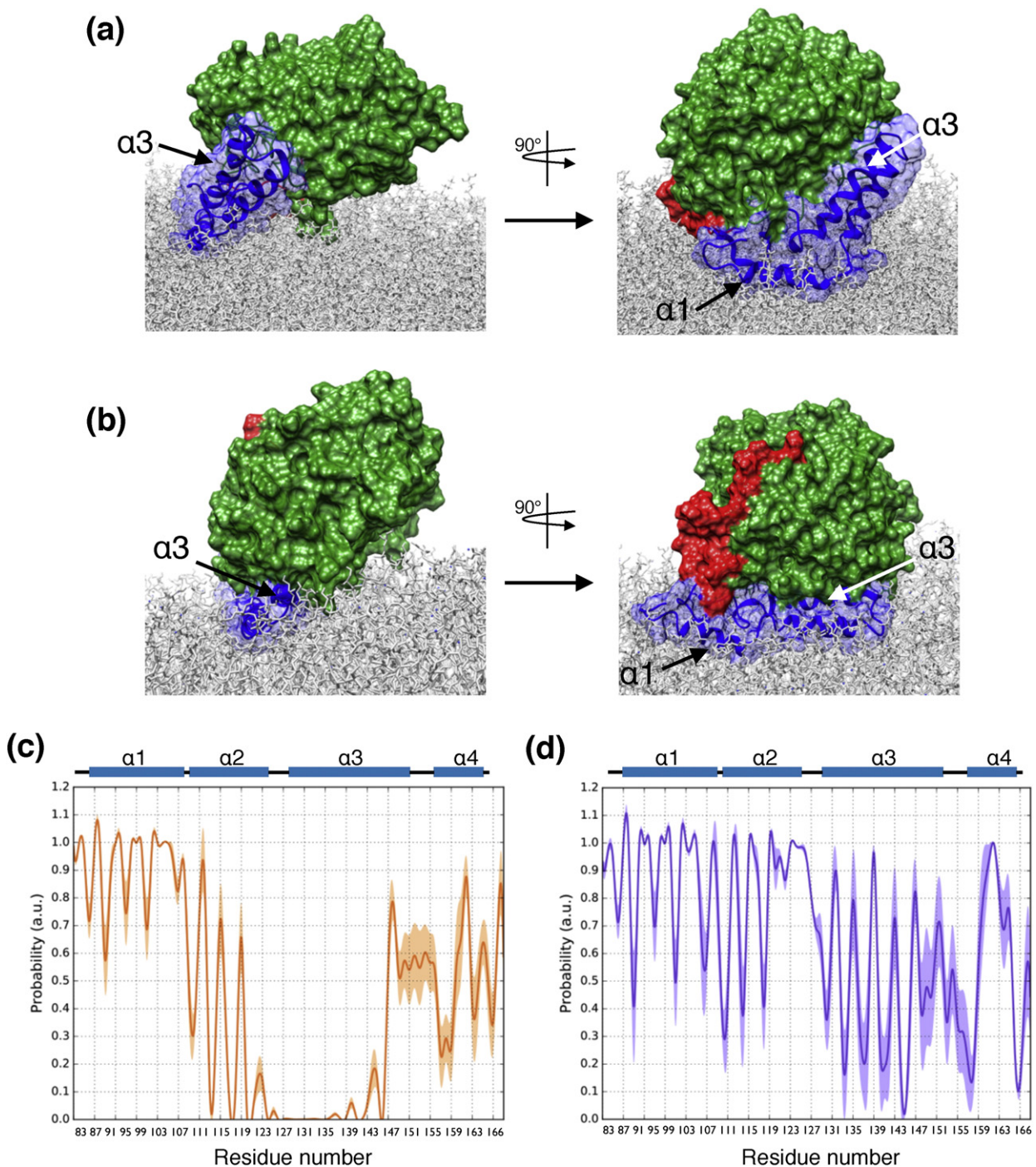
Interactions with a lipid bilayer

Simulations of a coarse-grained (CG) model were performed in the presence of a POPG bilayer. Fifteen independent 4 μs simulations were conducted starting from random orientations of the protein near the bilayer surface. In all but one of the

replicates, the saposin domain bound to the POPG surface, placing the catalytic domain in a "bowl down" orientation with the enzyme active site facing the lipid headgroups. Membrane contacts were predominantly with the saposin domain and there were weaker, transient interactions of the catalytic domain with the bilayer (Fig. 8). The density distribution of each component of the system along a membrane normal shows that the saposin domain localises in the headgroup region of the bilayer, and that the catalytic domain is more peripheral (Fig. S7).

The interactions between the saposin domain and the lipids were quantified by computing the fraction of time in which each saposin residue made at least one contact with any POPG molecule over the last 2.4 μs of each simulation. Two lipid-binding modes became apparent from this analysis (Fig. 8, C,D). The type I association was characterized by a partial insertion of the saposin into the headgroup region of the bilayer, but with few contacts of helix α3 with lipids. In the type II mode, the saposin hinge between the stem and hairpin regions was completely open, presenting the inside surface of all four helices to the bilayer. As in the all-atom simulations of ASM in solution, the saposin α3/catalytic domain contacts were maintained in all of the CG simulations, despite the conformational changes in the saposin domain and extensive interactions with the lipids.

Conclusions

ASM is a relatively non-sepcific phosphodiesterase that can hydrolyse the headgroup from sphingomyelin and various glycerophospholipids. The active site is found in the center of a shallow bowl with few

Fig. 8. Coarse-grained simulations of ASM with lipid bilayers identify two modes of saposin-lipid association. (a) Type I interactions are characterized by a partial membrane insertion of the saposin domain (blue), mostly involving helix 1 and excluding helix 3. The connector (red) and catalytic domain (green) make few contacts with the bilayer. (b) Type II interactions involve a fuller opening of the saposin domain exposing the inner hydrophobic surface of all four helices to the lipid environment. Close contacts between helix α3 and the catalytic domain are preserved in both type I and type II binding modes. (c,d) The averaged fraction of time a given residue of the saposin domain makes at least one contact with any POPG molecule in type I and II binding, respectively.

conserved polar residues near the di-zinc center that might dictate substrate specificity. The enzyme binds tightly to negatively charged membranes at acidic pH, and substrate specificity may be largely determined by which phosphodiester groups can gain access to the active site in the cellular setting. In the crystal structure,

the saposin domain is tightly associated with the catalytic domain, and we propose that this interface is maintained even upon saposin conformational changes in solution and at membrane surfaces. As a result, the saposin domain of ASM likely plays an important role in orienting the active site of the catalytic domain towards the membrane. This places the highly glycosylated back side of the bowl towards the aqueous solvent. The saposin fold is intrinsically flexible, and we suggest that the association of the saposin domain with membranes causes local deformations of the bilayer near the catalytic center, and that this disruption allows lipid phosphate groups to associate with the di-zinc center, positioning the target scissile phosphoester bond at the active site (Fig. 9). This proposed mechanism for ASM action may share features with other lysosomal lipid hydrolases that rely on separately encoded saposin proteins. Beta-glucosidase, for example, can bind to sites on

membranes that have been remodeled by saposin C, and the assembled complex is required for the breakdown of glucosylceramide at membrane surfaces [36]. Overall, the principles revealed from this structural analysis of ASM may be relevant to other enzymes that target membrane-embedded lipids.

Materials and methods

Protein expression and purification

Human acid sphingomyelinase (ASM; SMPD1; Uniprot ID P17405) was expressed with the *piggyBac* transposon-based mammalian cell expression system [21]. Codon optimized SMPD1 cDNA was purchased from Genescript® and a fragment coding for protein residues 47–629 was subcloned into the PB-T-PAF plasmid, which includes an
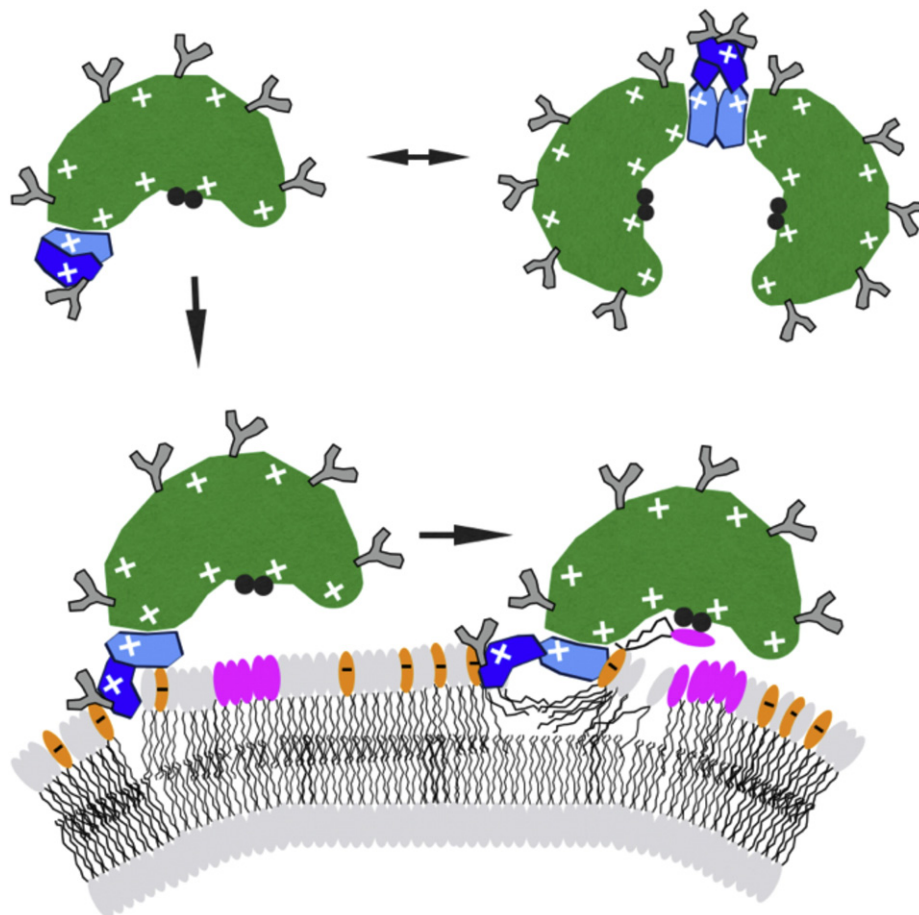
Fig. 9. Schematic of the ASM reaction at the surface of an intralysosomal vesicle. The stem and hairpin regions of the saposin domain are dark blue and light blue, respectively, and the catalytic domain is green. Gray "Y‴"s represent N-linked carbohydrates. Lipids with orange headgroups represent negatively charged BMP, and lipids with magenta headgroups represent substrates (SM or PC). In the soluble state, ASM exists in a monomer-dimer equilibrium according to the closed or open conformation of the saposin domain. In acidic conditions, the positively charged ASM monomer binds to negatively charged BMP-containing membranes. The opening of the saposin domain exposes the inner hydrophobic surface to the membrane and causes a local disruption of lipid packing, allowing the substrate headgroups access to the enzyme active site.

upstream N-terminal secretion signal and a Protein A (PA) purification tag followed by a tobacco etch virus (TEV) protease cleavage site. A mutation generating a C629S residue substitution was generated with the QuickChange site-directed mutagenesis kit (Stratagene). A mixture of the PB-T-PAF, PB-RB, and PBase plasmids at a ratio of 8:1:1 (1 μg total) was transfected into HEK293 GnT1$^{-/-}$ cells with Lipofectamine 2000 (Invitrogen). One day after transfection, the cells were trypsinized and distributed into fresh tissue culture plates. Dual drug selection with 10 μg/mL puromycin and 5 μg/mL blasticidin S in DMEM/F12 medium containing 10% *v*/v fetal bovine serum (FBS) was started at day 3 and continued until confluency. Drug-selected cells were distributed into a Nunc™ EasyFill™ Cell Factory System (Thermo Scientific) containing 500 mL DMEM/F12 medium supplemented with 10% *v*/v FBS. Once cells reached confluency, the medium was replaced with 800 mL DMEM/F12 medium with 1 μg/mL doxycycline (Sigma) to induce protein expression. The medium was harvested 4 days later and solid $(NH4)_2SO_4$ was added to 1 M. The solution was loaded onto a 5 mL HiTrap Phenyl HP column (GE Health), and protein was eluted with a linear gradient of elution buffer (25 mM HEPES, 10% *v*/v ethylene glycol, pH 7.5). Fractions containing the PA-ASM fusion were pooled, concentrated, and dialyzed against TEV reaction buffer (50 mM Tris–HCl, 1 mM EDTA, pH 8.0) overnight. TEV protease was then added and incubated at 4 °C overnight to release the ASM from the PA fusion tag. The sample was dialyzed against Q-Sepharose binding buffer (25 mM Tris–HCl, 100 mM NaCl, 1 mM zinc acetate, pH 8.0) and loaded onto a 5 mL Econo-Pac Q Cartridge (BioRad). ASM was collected in the flow through fractions and further purified by size exclusion chromatography on a SP_S200_16 column in 5 mM Tris–HCl, 50 mM NaCl, pH 7.0. Pooled ASM fractions were concentrated to 10 mg/mL and stored at −80 °C. The molecular weight of the purified protein was 72,834 Da by MALDI-TOF mass spectrometry, a value that agrees within 0.4% of the calculated value of 72,563 Da for residues 46–626 incorporating a C629S substitution and six (N-acetylglucosamine)$_2$(mannose)$_5$ glycosylation sites.

Crystallization and structure determination

Crystals were grow by vapor diffusion by mixing 1 μL protein solution, 0.5 μL seed solution consisting of crystalline seeds in 1 M sodium potassium tartrate, 0.1 M MES, pH 6.0, and 1.5 μL reservoir buffer (0.2 M sodium acetate, 20% *w*/v polyethylene glycol 8000, 0.1 M sodium cacodylate, pH 6.0), and equilibrating against 0.5 mL of reservoir solution. In our liposome-based assay conditions, ASM retains approximately half of its maximal activity at pH 6 (Fig. S5). Selenomethionine-substituted protein was expressed from the *piggyBac* transformed cells using the method described by Barton et al. [37], and purified and crystallized as with the native protein.

All diffraction data were collection at 100 K. For the native dataset, crystals were flash cooled without cryoprotectant with the high pressure cooling method [38] and diffraction data were collected at a wavelength of 0.63 Å at beamline A1 at Cornell High Energy Synchrotron Source (CHESS), Cornell University. For the selenomethionine-substituted protein, crystals were briefly soaked in well solution supplemented with 5% ethylene glycol prior to flash freezing, and diffraction data were collected at

wavelength of 0.979 Å at beamline 08ID-1 at the Canadian Macromolecular Crystallography Facility, Canadian Light Source. X-ray fluorescence excitation scans confirmed the presence of both Zn and Se in the crystals. Diffraction images were integrated with HKL 2000 [39] and scaled and merged with AIMLESS [40]. Initial phasing was done with Phenix MR-SAD [41] using a truncated model based on PDB entry 5EBE. Model rebuilding and refinement were carried out with Coot [42], Phenix [41] and the pdb.redo server [43]. The crystallographic statistics are presented in Table 1. Figures were produced with PyMOL [44] and Chimera [45]. The diffraction data were significantly anisotropic, and the scaled, unmerged data were truncated to a resolution of 3.4 Å, 3.0 Å and 2.8 Å along the a*, b* and c* directions, respectively, solely for the purpose of generating the data reduction statistics presented in the column "Elliptically truncated" of Table 1. The structure refinement was carried out on the non-truncated dataset, as recommended by the authors of Phenix [41]. The anisotropic resolution cutoffs were determined from the UCLA Diffraction Anisotropy Server [46], and correspond roughly to a CC1/2 of 0.5 in each of the reciprocal space directions. Software used in this project was curated by SBGrid [47].

Gel filtration chromatography

100 μL samples (15 μM or 50 μM) of ASM were injected onto a Bio-Rad Enrich SEC 650 30 10 mm column pre-equilibrated with either 150 mM NaCl, 50 mM HEPES pH 7 or 150 mM NaCl, 50 mM sodium acetate pH 5 and eluted at a flow rate of 1 mL/min.

Liposome binding

Liposomes were prepared by mixing indicated ratios of SM, PC, cholesterol and/or BMP (Avanti Polar Lipids) in chloroform and evaporating the solvent under N_2 gas. The lipid film was dispersed by vortex mixing in 5 mM Tris–HCl, pH 7.0 to 10 mM lipid. The suspension was submitted to 10 cycles of freezing and thawing and sonicated in a bath sonicator for 30 min. Liposomes were diluted to 2.5 mM in 100 μL in neutral buffer (50 mM MES, 150 mM NaCl, pH 7) or acidic buffer (50 mM sodium acetate, 150 mM NaCl, pH 4.8) and ASM was added to final concentration of 1 μM. After 5 min, the liposomes were pelleted by centrifugation at 21,000 Xg for 30 min at room temperature. The amount of ASM in the pellet and supernatant fractions were determined by densitometry of Coomassie-stained non-reducing SDS-PAGE.

Activity assay

ASM activity was quantified with the Amplex Red sphingomyelinase assay kit (Thermal Scientific). Liposomes were diluted to 0.5 mM and ASM was added to a final concentration of 0.2 μM with a total reaction volume of 10 μL. After a 20 min incubation at 37 °C, the reaction was stopped by adding 10 μL of the Amplex Red reaction mixture and incubated for 60 min at 37 °C. Test reactions were used to verify that the reaction rate was linear over the selected incubation time. The emission signal at

600 nm was measured with excitation at 530 nm. Standard curves were generated with 0–10 μM phosphocholine, and were not affected by the pH of the incubation reaction.

Molecular docking

Molecular modeling of the interactions between SM and ASM was done with the Small-Molecule Drug Discovery Suite 2016–1 from Schrödinger (http://www.schrodinger.com/smdd/). The protein structure was prepared using the Protein Preparation Wizard procedure and the ionization states of the protein side chains and Zn^{2+} were assigned at pH 5, and a ligand consisting of a SM analog with truncated acyl tails was prepared with LigPrep. The center and the size of the binding site were defined by manually positioning the phosphate oxygens of the ligand near the catalytic Zn^{2+}. Energy GRIDs were calculated in a box defined by adding 10 Å to each side of the ligand. The top 10 best scored poses from the Glide v. 7.0 docking program with a standard precision (SP) scoring function and the OPLS3 force field were visually inspected. While the protein was kept rigid during the docking stage, the ligand was fully flexible and we set 500 docked poses to undergo post-docking minimization prior to the final rescoring. The top scored pose was and was energy minimized with positional constraints on the protein backbone, Zn^{2+} cations and the SM phosphate group with a distance-dependent dielectric constant of 4 and a convergence threshold of 0.3.

Molecular dynamic simulations

All simulations were performed with GROMACS package 5.0.4. All-atom simulations of an ASM monomer in explicit water buffer were conducted using the CHARMM22star force field [48,49] with SPC/E water. Four replicas were used with a box size of $13 \times 13 \times 13$ nm^3 for each system. Five Na$^+$ ions were added to neutralize the system. Each system was prepared from a monomer of the ASM crystal structure and energy-minimized in 1000 steps using steepest descent, followed by a pre-equilibration phase of 100 ps with position restraints on the protein backbone using a force constant of 1000 kJ·mol^{-1}·nm^{-1}. A 64 ns simulation was conducted for each system using MD [50]. The aqueous solution and the protein were coupled separately in a temperature bath at 300 K with a coupling constant of 0.4 ps using the Nosé-Hoover algorithm. The pressure was set at 1 atm using the Parrinello-Rahman barostat with a semi-isotropic coupling scheme. Lennard-Jones interactions were cutoff at 1 nm and Coulomb interactions were calculated using the smooth particle-mesh Ewald method with a real-space cutoff of 1 nm and a Fourier grid spacing of 0.15 nm.

The MARTINI force field was used to carry out coarse-grained (CG) simulations of ASM with a lipid bilayer [51,52]. The atomistic model of the enzyme was converted to a CG representation based on four-to-one mapping by using the program martinize.py [53] and secondary structure assignment from DSSP [54]. By using the program insane.py, a total of 722 CG POPG lipids were divided and equally distributed between two membrane leaflets as pre-assembly bilayer configuration, and the protein was placed in the layer of polarizable CG water near the POPG lipid surface, with 15 random initial orientations. Both N- and C-termini of the protein were kept neutral while residues Arg, Lys and His were protonated to mimic an environment at pH 5. The Zn^{2+} ion inside the protein was replaced by Ca^{2+} to maintain electroneutrality because CG force field parameters for Zn^{2+} are not currently available. Harmonic bonds with a force constant of 9000 kJ·mol^{-1}·nm^{-1} were added to maintain the coordination of the metals with the protein. 703 water molecules were replaced with 703 Na$^+$ counterions to ensure system electroneutrality. The box size of all 15 systems was $14.5 \times 14.5 \times 9$ nm^3. Each system was first energy-minimized in 5000 steps using the steepest descent gradient. Two short 0.5 ns simulations, the first one with a very small time step (1 fs) and the second one with a slightly larger time step (10 fs), were conducted as pre-equilibration phases with position restraints on protein backbone using a force constant of 1000 kJ·mol^{-1}·nm^{-1}. A 10 ns simulation with the regular time step (20 fs) was then performed to equilibrate the box dimensions by using the semi-isotropic Berendsen barostat [55]. Subsequently, a 4000 ns simulation was conducted for each system, yielding a total simulation scale of 60 μs. For all CG simulations, the protein, POPG, and water were coupled separately in a temperature bath at 300 K with a coupling constant of $\tau_T = 1$ ps using the v-rescale algorithm while a semi-isotropic pressure coupling scheme using the Parrinello-Rahman algorithm was also employed. Lennard-Jones interactions were evaluated using a cutoff of 11 Å, and electrostatic interactions were shifted to zero between 0 and 11 Å. The coordinates and energies were saved every 200 ps. CG models were converted back to all atom representations for analysis and figure generation [56].

Accession number

Coordinates and structure factors for ASM have been deposited in the Protein Data Bank with accession number 5JG8.

Acknowledgments

Appendix A. Supplementary data

Supplementary data to this article can be found online at http://dx.doi.org/10.1016/j.jmb.2016.06.012.

References

[1] G. van Meer, D.R. Voelker, G.W. Feigenson, Membrane lipids: where they are and how they behave, Nat. Rev. Mol. Cell Biol. 9 (2008) 112–124.

[2] Y.A. Hannun, L.M. Obeid, Principles of bioactive lipid signalling: lessons from sphingolipids, Nat. Rev. Mol. Cell Biol. 9 (2008) 139–150.

[3] G. van Meer, J.C. Holthuis, Sphingolipid transport in eukaryotic cells, Biochim. Biophys. Acta Mol. Cell Biol. Lipids 1486 (2000) 145–170.

[4] H. Schulze, K. Sandhoff, Sphingolipids and lysosomal pathologies, Biochim. Biophys. Acta Mol. Cell Biol. Lipids 1841 (2014) 799–810.

[5] T. Kolter, K. Sandhoff, Principles of lysosomal membrane digestion: stimulation of sphingolipid degradation by sphingolipid activator proteins and anionic lysosomal lipids, Annu. Rev. Cell Dev. Biol. 21 (2005) 81–103.

[6] C.P. Ponting, Acid sphingomyelinase possesses a domain homologous to its activator proteins: saposins B and D, Protein Sci. 3 (1994) 359–361.

[7] E.H. Schuchman, Acid sphingomyelinase, cell membranes and human disease: lessons from Niemann-Pick disease, FEBS Lett. 584 (2010) 1895–1900.

[8] E. Gulbins, M. Palmada, M. Reichel, A. Lüth, C. Böhmer, D. Amato, C.P. Müller, C.H. Tischbirek, T.W. Groemer, G. Tabatabai, K.A. Becker, P. Tripal, S. Staedtler, T.F. Ackermann, J. van Brederode, C. Alzheimer, M. Weller, U.E. Lang, B. Kleuser, H. Grassmé, J. Kornhuber, Acid sphingomyelinase-ceramide system mediates effects of antidepressant drugs, Nat. Med. 19 (2013) 934–938.

[9] J.K. Lee, H.K. Jin, M.H. Park, B.-R. Kim, P.H. Lee, H. Nakauchi, J.E. Carter, X. He, E.H. Schuchman, J.-S. Bae, Acid sphingomyelinase modulates the autophagic process by controlling lysosomal biogenesis in Alzheimer's disease, J. Exp. Med. 211 (2014) 1551–1570.

[10] N.H.T. Petersen, O.D. Olsen, L. Groth-Pedersen, A.-M. Ellegaard, M. Bilgin, S. Redmer, M.S. Ostenfeld, D. Ulanet, T.H. Dovmark, A. Lønborg, S.D. Vindeløv, D. Hanahan, C. Arenz, C.S. Ejsing, T. Kirkegaard, M. Rohde, J. Nylandsted, M. Jäättelä, Transformation-associated changes in sphingolipid metabolism sensitize cells to lysosomal cell death induced by inhibitors of acid sphingomyelinase, Cancer Cell 24 (2013) 379–393.

[11] R.W. Jenkins, D. Canals, J. Idkowiak-Baldys, F. Simbari, P. Roddy, D.M. Perry, K. Kitatani, C. Luberto, Y.A. Hannun, Regulated secretion of acid sphingomyelinase: implications for selectivity of ceramide formation, J. Biol. Chem. 285 (2010) 35706–35718.

[12] J. Kornhuber, C. Rhein, C.P. Müller, C. Mühle, Secretory sphingomyelinase in health and disease, Biol. Chem. 396 (2015) 707–736.

[13] A. Wähe, B. Kasmapour, C. Schmaderer, D. Liebl, K. Sandhoff, A. Nykjaer, G. Griffiths, M.G. Gutierrez, Golgi-to-phagosome transport of acid sphingomyelinase and prosaposin is mediated by sortilin, J. Cell Sci. 123 (2010) 2502–2511.

[14] R.W. Jenkins, J. Idkowiak-Baldys, F. Simbari, D. Canals, P. Roddy, C.D. Riner, C.J. Clarke, Y.A. Hannun, A novel mechanism of lysosomal acid sphingomyelinase maturation: requirement for carboxyl-terminal proteolytic processing, J. Biol. Chem. 286 (2011) 3777–3788.

[15] T. Linke, G. Wilkening, S. Lansmann, H. Moczall, O. Bartelsen, J. Weisgerber, K. Sandhoff, Stimulation of acid sphingomyelinase activity by lysosomal lipids and sphingolipid activator proteins, Biol. Chem. 382 (2001) 283–290.

[16] V.O. Oninla, B. Breiden, J.O. Babalola, K. Sandhoff, Acid sphingomyelinase activity is regulated by membrane lipids and facilitates cholesterol transfer by NPC2, J. Lipid Res. 55 (2014) 2606–2619.

[17] S.J. Freeman, P. Shankaran, L.S. Wolfe, J.W. Callahan, Phosphatidylcholine and 4-methylumbelliferyl phosphorylcholine hydrolysis by purified placental sphingomyelinase, Can. J. Biochem. Cell Biol. 63 (1985) 272–277.

[18] L.E. Quintern, G. Weitz, H. Nehrkorn, J.M. Tager, A.W. Schram, K. Sandhoff, Acid sphingomyelinase from human urine: purification and characterization, Biochim. Biophys. Acta 922 (1987) 323–336.

[19] M. Traini, C.M. Quinn, C. Sandoval, E. Johansson, K. Schroder, M. Kockx, P.J. Meikle, W. Jessup, L. Kritharides, Sphingomyelin phosphodiesterase acid-like 3 A (SMPDL3A) is a novel nucleotide phosphodiesterase regulated by cholesterol in human macrophages, J. Biol. Chem. 289 (2014) 32895–32913.

[20] L.X. Heinz, C.L. Baumann, M.S. Köberlin, B. Snijder, R. Gawish, G. Shui, O. Sharif, I.M. Aspalter, A.C. Müller, R.K. Kandasamy, F.P. Breitwieser, A. Pichlmair, M. Bruckner, M. Rebsamen, S. Blüml, T. Karonitsch, A. Fauster, J. Colinge, K.L. Bennett, S. Knapp, M.R. Wenk, G. Superti-Furga, The Lipid-Modifying Enzyme SMPDL3B Negatively Regulates Innate Immunity, Cell Rep. 11 (2015) 1919–1928.

[21] Z. Li, I.P. Michael, D. Zhou, A. Nagy, J.M. Rini, Simple *piggyBac* transposon-based mammalian cell expression system for inducible protein production, Proc. Natl. Acad. Sci. 110 (2013) 5004–5009.

[22] H. Qiu, T. Edmunds, J. Baker-Malcolm, K.P. Karey, S. Estes, C. Schwarz, H. Hughes, S.M. Van Patten, Activation of human acid sphingomyelinase through modification or deletion of C-terminal cysteine, J. Biol. Chem. 278 (2003) 32744–32752.

[23] M. Kölzer, K. Ferlinz, O. Bartelsen, S.L. Hoops, F. Lang, K. Sandhoff, Functional characterization of the postulated intramolecular sphingolipid activator protein domain of human acid sphingomyelinase, Biol. Chem. 385 (2004) 1193–1195.

[24] K. Popovic, J. Holyoake, R. Pomès, G.G. Privé, Structure of saposin A lipoprotein discs, Proc. Natl. Acad. Sci. U. S. A. 109 (2012) 2908–2912.

[25] B.C. Bryksa, P. Bhaumik, E. Magracheva, D.C. De Moura, M. Kurylowicz, A. Zdanov, J.R. Dutcher, A. Wlodawer, R.Y. Yada, Structure and mechanism of the saposin-like domain of a plant aspartic protease, J. Biol. Chem. 286 (2011) 28265–28275.

[26] M. Rossmann, R. Schultz-Heienbrok, J. Behlke, N. Remmel, C. Alings, K. Sandhoff, W. Saenger, T. Maier, Crystal Structures of Human Saposins C and D: Implications for Lipid Recognition and Membrane Interactions, Structure 16 (2008) 809–817.

[27] V.E. Ahn, K.F. Faull, J.P. Whitelegge, A.L. Fluharty, G.G. Privé, Crystal structure of saposin B reveals a dimeric shell for lipid binding, Proc. Natl. Acad. Sci. U. S. A. 100 (2003) 38–43.

[28] V.E. Ahn, P. Leyko, J.-R. Alattia, L. Chen, G.G. Privé, Crystal structures of saposins A and C, Protein Sci. 15 (2006) 1849–1857.

[29] K. Popovic, G.G. Privé, Structures of the human ceramide activator protein saposin D, Acta Crystallogr. D. Biol. Crystallogr. 64 (2008) 589–594.

[30] S.M. Lim, K. Yeung, L. Trésaugues, T.H. Ling, P. Nordlund, The structure and catalytic mechanism of human sphingomyelin phosphodiesterase like 3a - an acid sphingomyelinase homologue with a novel nucleotide hydrolase activity, FEBS J. 283 (2016) 1107–1123.

[31] A. Gorelik, K. Illes, G. Superti-Furga, B. Nagar, Structural Basis for Nucleotide Hydrolysis by the Acid Sphingomyelinase-like Phosphodiesterase SMPDL3A, J. Biol. Chem. 291 (2016) 6376–6385.

[32] M.V. Airola, J.M. Tumolo, J. Snider, Y.A. Hannun, Identification and biochemical characterization of an acid sphingomyelinase-like protein from the bacterial plant pathogen Ralstonia solanacearum that hydrolyzes ATP to AMP but not sphingomyelin to ceramide, PLoS One 9 (2014) e105830.

[33] J. Kornhuber, C.P. Müller, K.A. Becker, M. Reichel, E. Gulbins, The ceramide system as a novel antidepressant target, Trends Pharmacol. Sci. 35 (2014) 293–304.

[34] R. Hurwitz, K. Ferlinz, K. Sandhoff, The tricyclic antidepressant desipramine causes proteolytic degradation of lysosomal sphingomyelinase in human fibroblasts, Biol. Chem. Hoppe Seyler 375 (1994) 447–450.

[35] S. Zampieri, M. Filocamo, A. Pianta, S. Lualdi, L. Gort, M.J. Coll, R. Sinnott, T. Geberhiwot, B. Bembi, A. Dardis, SMPD1 Mutation Update: Database and Comprehensive Analysis of Published and Novel Variants, Hum. Mutat. 37 (2016) 139–147.

[36] J.-R. Alattia, J.E. Shaw, C.M. Yip, G.G. Privé, Molecular imaging of membrane interfaces reveals mode of beta-glucosidase activation by saposin C, Proc. Natl. Acad. Sci. U. S. A. 104 (2007) 17394–17399.

[37] W.A. Barton, D. Tzvetkova-Robev, H. Erdjument-Bromage, P. Tempst, D.B. Nikolov, Highly efficient selenomethionine labeling of recombinant proteins produced in mammalian cells, Protein Sci. 15 (2006) 2008–2013.

[38] C.U. Kim, R. Kapfer, S.M. Gruner, High-pressure cooling of protein crystals without cryoprotectants, Acta Crystallogr. D. Biol. Crystallogr. 61 (2005) 881–890.

[39] Processing of X-ray diffraction data collected in oscillation mode, in: Z. Otwinowski, W. Minor, B.T.-M. in Enzymology (Eds.), Macromol. Crystallogr. Part A, Academic Press 1997, pp. 307–326.

[40] M.D. Winn, C.C. Ballard, K.D. Cowtan, E.J. Dodson, P. Emsley, P.R. Evans, R.M. Keegan, E.B. Krissinel, A.G.W. Leslie, A. McCoy, S.J. McNicholas, G.N. Murshudov, N.S. Pannu, E.A. Potterton, H.R. Powell, R.J. Read, A. Vagin, K.S. Wilson, Overview of the CCP 4 suite and current developments, Acta Crystallogr. Sect. D Biol. Crystallogr. 67 (2011) 235–242.

[41] P.D. Adams, P.V. Afonine, G. Bunkóczi, V.B. Chen, I.W. Davis, N. Echols, J.J. Headd, L.-W. Hung, G.J. Kapral, R.W. Grosse-Kunstleve, A.J. McCoy, N.W. Moriarty, R. Oeffner, R.J. Read, D.C. Richardson, J.S. Richardson, T.C. Terwilliger, P.H. Zwart, PHENIX : a comprehensive Python-based system for macromolecular structure solution, Acta Crystallogr. Sect. D Biol. Crystallogr. 66 (2010) 213–221.

[42] P. Emsley, B. Lohkamp, W.G. Scott, K. Cowtan, Features and development of Coot, Acta Crystallogr. Sect. D Biol. Crystallogr. 66 (2010) 486–501.

[43] R.P. Joosten, F. Long, G.N. Murshudov, A. Perrakis, The PDB_REDO server for macromolecular structure model optimization, IUCrJ. 1 (2014) 213–220.

[44] The PyMOL Molecular Graphics System, Version 1.8 Schrödinger, LLC

[45] E.F. Pettersen, T.D. Goddard, C.C. Huang, G.S. Couch, D.M. Greenblatt, E.C. Meng, T.E. Ferrin, UCSF Chimera-a visualization system for exploratory research and analysis, J. Comput. Chem. 25 (2004) 1605–1612.

[46] M. Strong, M.R. Sawaya, S. Wang, M. Phillips, D. Cascio, D. Eisenberg, Toward the structural genomics of complexes: crystal structure of a PE/PPE protein complex from Mycobacterium tuberculosis, Proc. Natl. Acad. Sci. U. S. A. 103 (2006) 8060–8065.

[47] A. Morin, B. Eisenbraun, J. Key, P.C. Sanschagrin, M.A. Timony, M. Ottaviano, P. Sliz, Collaboration gets the most out of software, Elife 2 (2013) e01456.

[48] P. Bjelkmar, P. Larsson, M.A. Cuendet, B. Hess, E. Lindahl, Implementation of the CHARMM Force Field in GROMACS: Analysis of Protein Stability Effects from Correction Maps, Virtual Interaction Sites, and Water Models, J. Chem. Theory Comput. 6 (2010) 459–466.

[49] S. Piana, K. Lindorff-Larsen, D.E. Shaw, How robust are protein folding simulations with respect to force field parameterization? Biophys. J. 100 (2011) 47–49.

[50] W.F. Van Gunsteren, H.J.C. Berendsen, A Leap-frog Algorithm for Stochastic Dynamics, Mol. Simul. 1 (1988) 173–185.

[51] S.J. Marrink, H.J. Risselada, S. Yefimov, D.P. Tieleman, A.H. de Vries, The MARTINI force field: coarse grained model for biomolecular simulations, J. Phys. Chem. B 111 (2007) 7812–7824.

[52] L. Monticelli, S.K. Kandasamy, X. Periole, R.G. Larson, D.P. Tieleman, S.-J. Marrink, The MARTINI Coarse-Grained Force Field: Extension to Proteins, J. Chem. Theory Comput. 4 (2008) 819–834.

[53] D.H. de Jong, G. Singh, W.F.D. Bennett, C. Arnarez, T.A. Wassenaar, L.V. Schäfer, X. Periole, D.P. Tieleman, S.J. Marrink, Improved Parameters for the Martini Coarse-Grained Protein Force Field, J. Chem. Theory Comput. 9 (2013) 687–697.

[54] W. Kabsch, C. Sander, Dictionary of protein secondary structure: pattern recognition of hydrogen-bonded and geometrical features, Biopolymers 22 (1983) 2577–2637.

[55] H.J.C. Berendsen, J.P.M. Postma, W.F. van Gunsteren, A. DiNola, J.R. Haak, Molecular dynamics with coupling to an external bath, J. Chem. Phys. 81 (1984) 3684–3690.

[56] T.A. Wassenaar, K. Pluhackova, R.A. Böckmann, S.J. Marrink, D.P. Tieleman, Going Backward: A Flexible Geometric Approach to Reverse Transformation from Coarse Grained to Atomistic Models, J. Chem. Theory Comput. 10 (2014) 676–690.